



# A comparative laboratory study of soft X-ray-induced ionization and fragmentation of five small PAH cations

Yining Huo<sup>1</sup>, Mónica K. Espinoza Cangahuala<sup>1</sup>, Vicente Zamudio-Bayer<sup>2</sup> , Marcelo Goulart<sup>1</sup>, Markus Kubin<sup>2</sup>, Martin Timm<sup>2</sup>, J. Tobias Lau<sup>2,3</sup>, Bernd von Issendorff<sup>3</sup>, Ronnie Hoekstra<sup>1,4</sup>, Shirin Faraji<sup>1</sup>, and Thomas Schlathölter<sup>1,5,a</sup>

<sup>1</sup> Zernike Institute for Advanced Materials, University of Groningen, Nijenborgh 4, 9747 AG Groningen, The Netherlands  
<sup>2</sup> Abteilung für Hochempfindliche Röntgenspektroskopie, Helmholtz-Zentrum Berlin für Materialien und Energie, Albert-Einstein-Str. 15, 12489 Berlin, Germany  
<sup>3</sup> Physikalisches Institut, Albert-Ludwigs-Universität Freiburg, Hermann-Herder-Str. 3, 79104 Freiburg, Germany  
<sup>4</sup> Advanced Research Center for Nanolithography (ARCNL), Science Park 106, 1098 XG Amsterdam, The Netherlands  
<sup>5</sup> University College Groningen, University of Groningen, Hoendiepskade 23/24, 9718 BG Groningen, The Netherlands

Received 14 July 2023 / Accepted 25 September 2023 / Published online 16 October 2023  
© The Author(s) 2023

**Abstract.** The interaction between polycyclic aromatic hydrocarbon (PAH) radical cations and X-rays predominantly leads to photofragmentation, a process that strongly depends on PAH size and geometry. In our experiments, five prototypical PAHs were exposed to monochromatic soft X-ray photons with energies in the C K-edge regime. As a function of soft X-ray photon energy, photoion yields were obtained by means of time-of-flight mass spectrometry. The resulting near-edge X-ray absorption mass spectra were interpreted using time-dependent density functional theory (TD-DFT) with a short-range corrected functional. We found that the carbon backbone of anthracene<sup>+</sup> (C<sub>14</sub>H<sub>10</sub><sup>+</sup>), pyrene<sup>+</sup> (C<sub>16</sub>H<sub>10</sub><sup>+</sup>) and coronene<sup>+</sup> (C<sub>24</sub>H<sub>12</sub><sup>+</sup>) can survive soft X-ray absorption, even though mostly intermediate size fragments are formed. In contrast, for hexahydropyrene<sup>+</sup> (C<sub>16</sub>H<sub>16</sub><sup>+</sup>) and triphenylene<sup>+</sup> (C<sub>18</sub>H<sub>12</sub><sup>+</sup>) molecular survival is not observed and the fragmentation pattern is dominated by small fragments. For a given excitation energy, molecular survival evidently does not simply correlate with PAH size but strongly depends on other PAH properties.

## 1 Introduction

Polycyclic aromatic hydrocarbons (PAHs) are a family of organic molecules consisting of multiple 6-membered carbon rings and are thought to be widely distributed throughout the interstellar medium (ISM) in neutral as well as in ionic form. In the ISM, PAHs get photoexcited mostly by ultraviolet (UV) and vacuum ultraviolet (VUV) photons. After internal conversion and intramolecular vibrational redistribution, the resulting vibrationally hot PAHs relax predominantly by emission of infrared (IR) photons [1, 2].

UV and in particular VUV photoexcited PAHs can also suffer dissociation/fragmentation, with the fragmentation pattern again depending on PAH structure [3, 4], size [4, 5], aliphatic side group [6] and state of hydrogenation [7]. In molecular clouds that surround astronomical X-ray sources, such as planetary nebulae (PNe) [8–10], supernova remnants [11, 12], active galactic nuclei [13–17] and young stellar objects [18, 19],

X-ray photoabsorption processes are relevant. Here, photofragmentation is dominating, at least for small PAHs.

Over the last years, we have thoroughly investigated the interaction of soft X-ray photons with energies around the carbon K-edge with gas-phase coronene cations and their singly and multiply hydrogenated counterparts [20–22]. In these studies, we employed near-edge X-ray absorption mass spectrometry (NEXAMS) [23], a technique in which partial photofragment ion yields as a function of X-ray photon energy are recorded, by exposure of molecular ions to monochromatic soft X-rays. Using time-dependent density functional theory (TD-DFT) calculations, C 1s core excitation to specific unoccupied molecular orbitals could be assigned to resonant features in the NEXAMS spectra. The NEXAMS studies showed that soft X-ray excitation as well as direct ionization into the continuum could induce non-dissociative ionization (NDI) but with very small probability. Instead, H/H<sub>2</sub> loss as well as carbon backbone fragmentation are dominating. Backbone fragmentation was found to be substantially reduced for hydrogenated coronene precursor cations [22]. In subsequent studies on (significantly smaller) pyrene

**Supplementary Information** The online version contains supplementary material available at <https://doi.org/10.1140/epjd/s10053-023-00763-w>.

<sup>a</sup> e-mail: [t.a.schlatholter@rug.nl](mailto:t.a.schlatholter@rug.nl) (corresponding author)

**Table 1** List of the five PAHs studied and the abbreviations used throughout the paper

Molecule	Abbreviation	Formula	Mass (Da)
Anthracene	Ant	C <sub>14</sub> H <sub>10</sub>	178
Pyrene	Py	C <sub>16</sub> H <sub>10</sub>	202
Hexahdropyrene	Hpy	C <sub>16</sub> H <sub>16</sub>	208
Triphenylene	Tpl	C <sub>18</sub> H <sub>12</sub>	228
Coronene	Cor	C <sub>24</sub> H <sub>12</sub>	300

cations and their superhydrogenated counterparts, H-attachment was found to have the opposite effect [24].

Here, we extend our investigation of coronene and pyrene cations by a systematic NEXAMS study of five different prototypical PAH cations, anthracene (ant), pyrene (py), 1,2,3,6,7,8-hexahdropyrene (hpy), triphenylene (tpl) and coronene (cor), see Table 1. Ant is a typical catacondensed PAH of linear geometry, while py and cor are both pericondensed PAHs. Tpl is a special catacondensed PAH where no C atom belongs to three benzene rings. The symmetry of the molecules increases from D<sub>2h</sub> (ant, py), D<sub>3h</sub> (tpl) to D<sub>6h</sub> (cor). The fifth molecule, hpy, is not a regular PAH, but it is the sixfold hydrogenated form of py. The hydrogenation leads to a significantly perturbed planar structure and symmetry as compared to py. We have included hpy in this study, as its activation by other methods has been thoroughly investigated previously [25, 26].

The carbon K-edge NEXAMS spectra are interpreted and discussed with the help of TD-DFT calculations.

## 2 Methods

### 2.1 NEXAMS experiments

The experiments were carried out using the Ion Trap endstation that is attached to the UE52-PGM beamline of the BESSY II synchrotron facility (Helmholtz-Zentrum Berlin für Materialien und Energie, Berlin, Germany) [27, 28]. All chemicals were purchased from Sigma-Aldrich in high purity of at least 99% and mixed with HPLC-grade methanol in order to obtain saturated solutions. The saturated PAH solutions were then diluted with methanol, and 10 mmol/L AgNO<sub>3</sub> was added to facilitate the formation of radical PAH cations based on the reaction process: PAH+Ag<sup>+</sup> → Ag+PAH<sup>+</sup>.

The cationic PAH molecules were brought to the gas phase by means of electrospray ionization (ESI). The electrosprayed PAH cations were then phase space compressed in an RF ion funnel. The beam of molecular ions coming out from the RF funnel was mass-selected by a quadrupole mass filter and electrostatically deflected by 90°. Eventually, the deflected ions were trapped in a cryogenic (≈ 20 K) quadrupole RF ion trap. Monochromatic soft X-ray beams from the BESSY II synchrotron passed axially through the linear RF trap containing the PAH cations. The soft X-ray photon energy was

ramped from 279 eV to 300 eV with a resolution of 50 meV, and the generated photoproducts were extracted into a reflectron time-of-flight (TOF) mass spectrometer where they were detected on a microchannel plate (MCP) detector and their times of arrival registered. From the obtained TOF mass spectra, partial fragmentation yields were obtained as a function of photon energy,  $E_{X-ray}$ .

### 2.2 TD-DFT computations

An efficient and accurate method of computing near-edge soft X-ray absorption spectra is TD-DFT using short-range corrected (SRC) functionals [29, 30]. All calculations were performed using the Q-Chem 5.2.2 [31] quantum chemistry program package. The geometry optimization and frequency analysis (to check for imaginary vibrational frequencies) were done at the  $\omega$ B97XD/cc-pVDZ theory level for all PAH cations. Finally, a single point calculation was performed to obtain the vertical core excitation energies at the SRC-2-R1-D2/cc-pVDZ theory level. This functional is most suitable to calculate the absorption spectra within the Tamm–Dancoff approximation [32]. For all PAHs, 1000 transitions from K-shell to higher excited electronic states were computed. The energy range covered the entire excitation region up to more than 295 eV.

## 3 Results and discussion

### 3.1 Photofragmentation mass spectra

The fragmentation pattern of a PAH at a given X-ray photon energy is a fingerprint of the photoabsorption-induced dynamics. In all the five PAH cations under study here, photons with energies just above the C K-edge ( $E_{X-ray} \approx 285$  eV) can drive C 1s transitions to low-lying unoccupied molecular orbitals. The resulting 1s vacancy is then predominantly filled by Auger-deexcitation, a process in which at least one (Auger) electron is emitted [20, 33]. This implies that after photon absorption and subsequent Auger decay, the PAH cation is predominantly left in a doubly ionized state, though a small fraction of triply ionized PAH cations can be present. The doubly ionized product of the Auger decay process will usually have a substantial electronic excitation, depending on the molecular orbital from which the decaying electron originated and left a vacancy. As described in the work of Egorov et al. [34], the average electronic excitation energy after Auger decay can be determined from the Auger electron spectrum. We are not aware of any Auger electron spectra for PAHs or PAH cations in the scientific literature. However, Auger spectra for gas-phase benzene are available in the literature [35].

The KVV (K indicates the initial vacancy site and V indicates the initial valence sites at the two active electrons) Auger spectrum of benzene covers an excitation

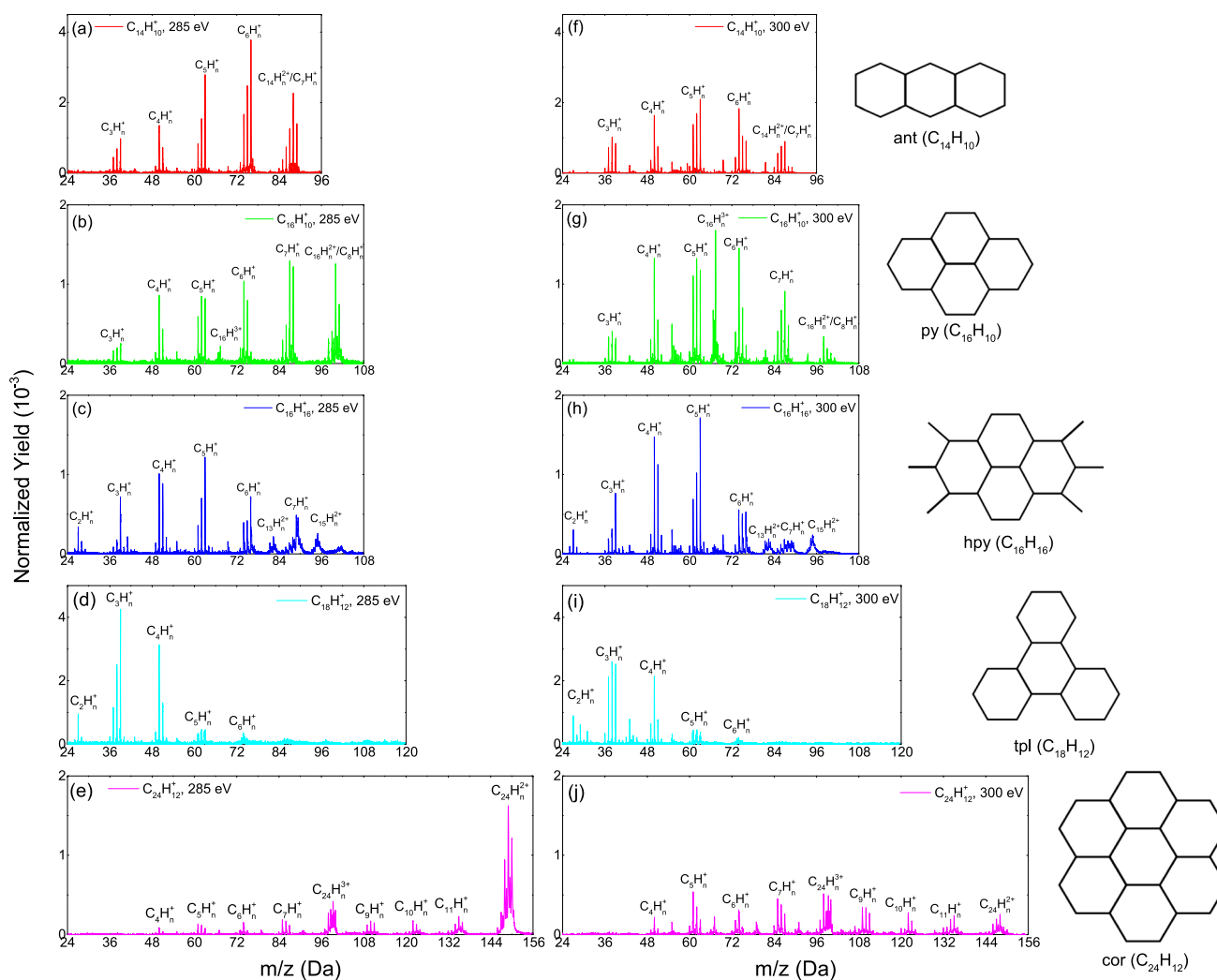


**Fig. 1** Photofragmentation spectra of ant **a, f**, py **b, g**, hpy **c, h**, tpl **d, i** and cor **e, j** cations induced by 285 eV photons (left column) and 300 eV photons (right column). The spectra are normalized to the respective yields of all photoproducts. The insets show the molecular structure of each of the 5 PAHs. More detailed and wide-range mass spectra are presented in the supplementary material

energy range from 0 to about 50 eV, with an average excitation of about 17.3 eV [36]. Via internal conversion and intramolecular vibrational redistribution, this energy will eventually determine the internal temperature of the resulting molecular dications. Using the method from Micelotta et al. [37], the average excitation energy can be related to an effective PAH temperature of  $\sim 2050$  K ( $\text{ant}^+$ ),  $\sim 1940$  K ( $\text{py}^+$ ),  $\sim 2000$  K ( $\text{hpy}^+$ ),  $\sim 1850$  K ( $\text{tpl}^+$ ) and  $\sim 1650$  K ( $\text{cor}^+$ ).

The fragmentation of these hot intermediate PAH dications determines the experimentally observed fragmentation patterns, presented in Fig. 1, which show  $E_{X\text{-ray}} = 285$  eV photoabsorption products from  $m/z = 24$  to just above  $m/z \approx M/2$  in the left panel ( $M$  being the precursor cation mass). Fragments with larger  $m/z$  are only observed with very small relative cross sections. Such fragments could in principle be formed in asymmetric fragmentation processes that involve charge separation, but for all five PAH

molecules under study, these channels appear to be very weak.

This implies that the fragments observed in Fig. 1 result primarily from neutral H, H<sub>2</sub> or C<sub>2</sub>H<sub>n</sub> loss from the intermediate PAH dication and/or from multifragmentation into small neutral and singly charged fragments. Finally, before discussing the molecule specific fragmentation spectra, it is important to realize that the presented mass spectra have been recorded from an RF ion trap. Trapping efficiencies are inherently  $m/z$ -dependent, with low efficiency at low  $m/z$ . The decrease in peak intensities at low  $m/z$  might therefore be an experimental artefact. However, exact knowledge on the reduction of detection efficiencies at low  $m/z$  values is not necessary as the main focus of this work is the comparison of the photofragmentation patterns of five different PAH molecules.

The clearest difference between the 5 PAH molecules is the presence or absence of a dicationic, non-dissociative

single ionization (NDSI) peak at  $m/z = M/2$  and of a tricationic non-dissociative double ionization (NDDI) peak at  $m/z = M/3$ . For  $\text{ant}^+$ ,  $\text{py}^+$  and  $\text{cor}^+$ , non-dissociative ionization (NDI) is clearly observed, whereas for  $\text{hpy}^+$  and  $\text{tpl}^+$  no signs of NDI can be found. Given that the masses of  $\text{hpy}^+$  and  $\text{tpl}^+$  are in between  $\text{ant}^+$  and  $\text{cor}^+$ , the NDI channel is not just an effect of the size of the precursor molecule (and therefore its vibrational degrees of freedom and effective temperature after photoexcitation) but rather a signature of lower structural stability of  $\text{hpy}^+$  and  $\text{tpl}^+$ .

A common feature of all spectra is the lack of large fragments. Precursor molecules either stay intact or lose on or more hydrogen atoms, or they break apart in relatively small fragments. The absence of large fragments could indicate a bimodal internal energy distribution. Another very important aspect is the possibility of cooling of the photoionized intermediate di- or trications by means of recurrent fluorescence (or Poincaré fluorescence [38]). In this process, vibrational energy can be transferred back into electronic degrees of freedom. The resulting electronically excited states then decay radiatively, under emission of photons that typically have UV energies. Martin et al. have observed this cooling process, for instance, for anthracene dications [39]. It is important to realize, however, that recurrent fluorescence is a process that involves ms timescales.

In our studies, the ions are held in a trap that is filled with cryogenic He buffer gas. Collisional cooling is therefore acting on much shorter timescales ( $\mu\text{s}$ ) which is why recurrent fluorescence is not likely to contribute strongly to the observed mass spectra. On the other hand, the presence of  $\mu\text{s}$  collisional cooling offers a straightforward explanation for the quenched large fragments: low excitation energy processes that would lead to such large processes have relatively low decay rates. The process is therefore not likely to happen before the vibrational energy is cooled off.

### 3.1.1 Anthracene ( $\text{C}_{14}\text{H}_{10}^+$ , $m/z = 178$ )

Figure 1a shows the data for  $\text{ant}^+$ , which shows the typical groups of  $\text{C}_N\text{H}_n^{z+}$  peaks. Postma et al. have thoroughly discussed anthracene fragmentation patterns obtained from collisions with keV ions [40], where qualitatively similar fragmentation spectra were observed. In a nutshell, monocations ( $z = 1$ ) are dominating the spectra and the 5 strong groups of peaks are due to  $N = 3, 4, 5, 6$  and 7. Different numbers of H atoms  $n$  appear at integer mass numbers. In particular, for the  $N = 5, 6$  and 7 monocation groups, much weaker peaks at half-integer masses can be observed in between the integer mass peaks. These peaks are fingerprints of dicationic photoproducts. It is difficult to quantify the monocation/dication ratio because only dications with odd mass numbers can be unambiguously identified. The even numbered dications coincide with monocations. It is therefore also impossible to directly deter-

mine the relative cross section for NDI:  $\text{C}_{14}\text{H}_{10}^{2+}$  coincides with  $\text{C}_7\text{H}_5^+$  at an  $m/z = 89$ . However, the mass spectrum also features half-integer peaks at 88.5 and 87.5 which are fingerprints of  $\text{C}_{14}\text{H}_9^{2+}$  and  $\text{C}_{14}\text{H}_7^{2+}$  dications. These dication peaks are obviously weaker than the peaks at  $m/z = 88, 87, 86$ , corresponding to the  $\text{C}_{14}\text{H}_8^{2+}/\text{C}_7\text{H}_4^+$ ,  $\text{C}_{14}\text{H}_6^{2+}/\text{C}_7\text{H}_3^+$  and  $\text{C}_{14}\text{H}_4^{2+}/\text{C}_7\text{H}_2^+$ . Very likely, contributions from monocationic fragments are stronger than those from dications in this group of peaks.

This is in line with the finding that dicationic fragments with odd  $N$  (such as  $\text{C}_{13}\text{H}_n^{2+}$ ) are almost fully quenched. Instead, the spectrum is dominated by the monocation groups  $\text{C}_N\text{H}_n^+$  ( $N = 3, 4, 5, 6, 7$ ) with  $N = 6$  being strongest.

Figure 1f shows the corresponding data for 300 eV photon absorption, i.e. for carbon 1s ionization into the continuum. Clearly, the yields for the larger fragments  $\text{C}_7\text{H}_n^+$  and  $\text{C}_6\text{H}_n^+$  decrease, while the intensities of  $\text{C}_4\text{H}_n^+$  and  $\text{C}_3\text{H}_n^+$  increase.  $\text{C}_5\text{H}_n^+$  becomes the dominant fragments. More small fragments are induced by high-energy photons because more energy is deposited. A group of dicationic fragments ( $\text{C}_9\text{H}_n^{2+}$ ) appears, whereas the peaks due to  $\text{C}_{14}\text{H}_7^{2+}$  and  $\text{C}_{14}\text{H}_9^{2+}$  are quenched. Only very small yields of tricationic interaction products such as  $\text{ant}^{3+}$  ( $m/z = 59.4$ ) are observed. Theoretical data by Holm et al. predicted that 2+ is the highest anthracene charge state that is thermodynamically stable [41].

### 3.1.2 Pyrene ( $\text{C}_{16}\text{H}_{10}^+$ , $m/z = 202$ )

Py is the smallest pericondensed PAH, consisting of 4 benzene rings. The mass spectrum for 285 eV photons in Fig. 1b ( $E_{X\text{-ray}} = 285$  eV) features strong groups of monocationic  $\text{C}_N\text{H}_n^+$  ( $N = 3, 4, 5, 6, 7, 8$ ) with  $N = 7$  being strongest, i.e. the spectral features resemble those observed for  $\text{ant}^+$ .

Again, the group including the dicationic precursor ( $\text{C}_{16}\text{H}_n^{2+}$ ,  $m/z = 98$  to  $m/z = 101$ ) coincides with the corresponding monocationic group ( $\text{C}_8\text{H}_n^+$ ). Evidence for dication formation is once again dication peaks with odd numbers of H atoms  $n$  (e.g.  $\text{C}_{16}\text{H}_9^{2+}$  and  $\text{C}_{16}\text{H}_7^{2+}$  at  $m/z = 100.5$  and  $m/z = 99.5$ ).

It is interesting that evidence for NDDI into tricationic  $\text{C}_{16}\text{H}_{10}^{3+}$  ( $m/z = 67.36$ ) as well as multiple H-loss from this peak into  $\text{C}_{16}\text{H}_n^{3+}$  can be observed. Double ionization can, for instance, be due to double Auger decay, or due to electron impact ionization ‘from within’, where the outgoing Auger electron further ionizes the same molecule [42].

For  $E_{X\text{-ray}} = 300$  eV, the fragmentation pattern again shifts to smaller masses but in a more drastic way as compared to  $\text{ant}^+$ .  $\text{C}_{16}\text{H}_n^{2+}$  yields are substantially quenched but the group of  $\text{C}_{16}\text{H}_n^{3+}$  trications exhibits the expected strong increase.  $\text{Py}^{z+}$  ions are expected to be thermodynamically stable up to a charge state of 3+ [41].

### 3.1.3 Hexahydropyrene ( $C_{16}H_{16}^+$ , $m/z = 208$ )

The molecular structure of  $hpy^+$  is similar to that of  $py^+$  in the sense that both molecules share a similar backbone consisting of 16 carbon atoms. However, the addition of 6 hydrogen atoms adds aliphatic character to the molecule that, for instance, breaks the planarity that is typical for PAHs (the outer edge carbon atoms on the long axis are out of plane with the other carbon atoms) but also reduces stability. The fragmentation pattern in Fig. 1c ( $E_{X-ray} = 285$  eV) reflects these changes. First of all, the monocationic  $C_NH_n^+$  ( $N = 2, 3, 4, 5, 6, 7, 8$ ) fragmentation pattern is shifted dramatically towards smaller monocationic fragments, with  $N = 5$  being strongest. The group with  $N = 7$  is already strongly reduced in intensity, and the group with  $N = 8$  can be barely distinguished from the superimposed dication distribution. Under the assumption of a statistical (multi)fragmentation mechanism, the shift to smaller masses can be due to a higher vibrational temperature prior to fragmentation [43]. This can be ruled out as the excitation energy that remains in the molecular ion after photoabsorption and Auger decay is not expected to differ much between  $py^+$  and  $hpy^+$ . Due to its larger number of degrees of freedom, most likely  $hpy^+$  will therefore feature a lower vibrational temperature than  $py^+$ . The alternative explanation for the shift is the overall reduced structural stability in  $hpy^+$  as compared to  $py^+$ : Gatchell et al. [44] have shown that fast backbone fragmentation of  $hpy^+$  sets in at vibrational energies of about 13 eV, whereas for  $py^+$  this threshold is at about 15 eV.

It is very interesting to note that on the other hand, the additional hydrogen atoms can also lead to backbone stabilization: Fig. 1c shows evidence for formation of large dicationic fragments:  $C_{13}H_n^{2+}$  and  $C_{15}H_n^{2+}$  can be unambiguously identified, and evidence for  $C_{14}H_n^{2+}$  and  $C_{16}H_n^{2+}$  can be found for odd  $n$ , leading to peaks at non-integer  $m/z$ . In general, dication yields are much stronger for  $hpy^+$  than for  $py^+$ , i.e. the additional H atoms help to stabilize the double positive charge. No evidence for  $C_{16}H_n^{3+}$  trications can be observed, though.

For a photon energy of 300 eV [see Fig. 1h], the intensities of  $C_NH_n^+$  ( $N = 3, 4, 5$ ) increase and the intensity of  $C_7H_n^+$  is strongly reduced. The fragmentation pattern clearly shifts towards smaller masses. The intensities of large dicationic fragments  $C_{13}H_n^{2+}$  and  $C_{15}H_n^{2+}$  are very similar as for 285 eV. At about  $m/z = 55$ , a group of dicationic  $C_9H_n^{2+}$  is evidence for smaller doubly charged fragments. Around  $m/z = 67$  traces of tricationic fragments  $C_{16}H_n^{3+}$  can be identified.

### 3.1.4 Triphenylene ( $C_{18}H_{12}^+$ , $m/z = 228$ )

Figure 1d shows the  $E_{X-ray} = 285$  eV photofragmentation spectrum for  $tpl^+$ , which has a very open structure that only consists of edge carbon sites. Even though this molecule contains 2 more carbon atoms than  $py^+$  and it is a regular PAH, the fragmentation pattern is remarkable. Once again, monocationic  $C_NH_n^+$

( $N = 2, 3, 4, 5, 6, 7, 8$ ) fragments dominate, but large ion yields are only found for  $N = 3$  and  $N = 4$ , with  $N = 3$  being largest. The yields drop quickly with  $N$ , suggesting a much lower structural stability than all other systems under study, here. Furthermore, no dicationic  $C_NH_n^{2+}$  groups are observed at all.

Above the C 1s ionization threshold, the mass spectrum remains remarkably unchanged, with a slight increase of  $C_2H_n^+$  fragments. In addition, traces of dicationic fragments  $C_7H_n^{2+}$  and  $C_9H_n^{2+}$  are observed.

### 3.1.5 Coronene ( $C_{24}H_{12}^+$ , $m/z = 300$ )

Figure 1e shows the  $E_{X-ray} = 285$  eV photofragmentation spectrum for  $cor^+$ , the largest PAH cation under study here. We have described this spectrum in detail in a previous article [22]. The dominating group of peaks is due to NDSI into  $C_{24}H_{12}^{2+}$  and H-loss from this ion into  $C_{24}H_n^{2+}$ . Clearly,  $cor^+$  is sufficiently large to dissipate the excitation energy and yet stabilize the two positive charges. The second most intense group of peaks corresponds to tricationic  $C_{24}H_n^{3+}$ . Monocationic  $C_NH_n^+$  ( $N = 4, 5, 6, 7, 8, 10, 11, 12$ ) are observed at lower intensities, with the peaks for  $N = 8$  and  $N = 12$  being superimposed with trications and dications. The monocation peaks have comparable intensities for  $N = 7 - 11$ . It is clearly shown that intensities of  $C_{24}H_n^{2+}$  are much higher than other fragments. In excitation-Auger regime (below ionization threshold), the carbon backbone is mainly preserved for  $cor^+$ .

Figure 1j shows the  $cor^+$  photofragmentation spectrum for  $E_{X-ray} = 300$  eV. As expected, the yield of  $C_{24}H_n^{2+}$  cations drops dramatically. On the other hand, the yield of tricationic  $C_{24}H_n^{3+}$  only increases moderately. In comparison with the data, e.g.  $py^+$ , a moderate increase is remarkable, as  $cor^{3+}$  (and even  $cor^{4+}$ ) are thermodynamically stable [41]. In addition, evidence for dicationic smaller fragments, such as  $C_NH_n^{2+}$  ( $N = 9, 11, 13, 15$ ), is observed.

## 3.2 NEXAMS spectra and theoretical data

As shown in the last section, evidence for both NDSI and NDDI can be observed for  $ant^+$ ,  $py^+$  and  $cor^+$ . Figure 2 displays the corresponding NEXAMS data, i.e. the photon energy dependence of the respective partial ion yields, for  $C_{14}H_{10}^{2+/3+}$  (a, d), for  $C_{16}H_{10}^{2+/3+}$  (b, e) and for  $C_{24}H_{12}^{2+/3+}$  (c, f).

We will first focus on the dication yields in the left column, i.e. on NDSI. The first major peak at about 282.5 eV is due to C 1s transitions to the singly occupied molecular orbital (SOMO). (All PAH cations under study here are radical cations.) There is virtually no difference in C 1s-SOMO transition energy between the  $ant^+$ ,  $py^+$  and  $cor^+$ .

The peaks around 285 eV are due to carbon 1s- $\pi^*$  transitions. For anthracene, these  $\pi^*$  transitions are split into two peaks at about 284.5 eV and 286 eV. For  $py^+$ , these two peaks are distinguishable as well,

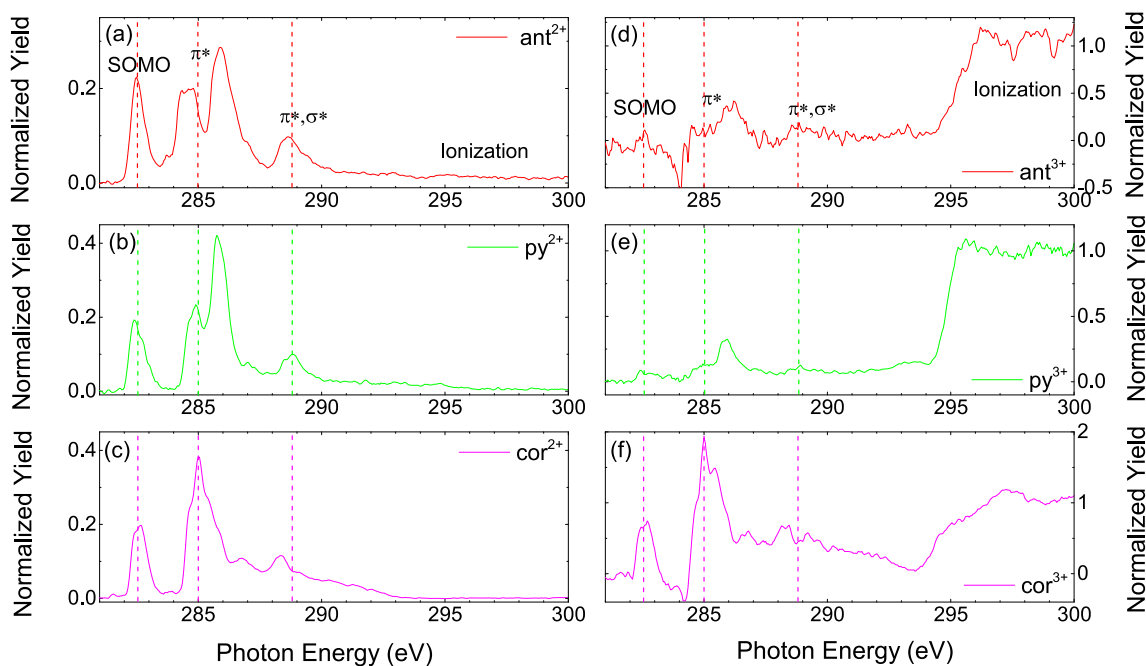


**Fig. 2** NEXAMS scans for NDSI (left) and NDDI (right). **a**  $C_{14}H_{10}^{2+}$ , **b**  $C_{16}H_{10}^{2+}$ , **c**  $C_{24}H_{12}^{2+}$ , **d**  $C_{14}H_{10}^{3+}$ , **e**  $C_{16}H_{10}^{3+}$ , **f**  $C_{24}H_{12}^{3+}$ . The dicationic spectra are normalized to the total yield of excitation regime, and the tricationic spectra are normalized to the average yield in the ionization regime. The data for the dications **a-c** also contain a small contribution of monocations with the same  $m/z$

but much less separated. For  $cor^+$ , both peaks merge into a single structure. These changes illustrate the differences in electronic structure between molecules. It is important to note that the  $1s-\pi^*$  peaks are actually due to a large number of  $1s-\pi^*$  transitions that cannot be resolved experimentally (see Fig. 3).

A weaker peak at about 288.5 eV is observed for all three molecules, as well.

At even higher photon energies, the NDSI yields decrease to very low values. Nonzero NDSI yields in the  $1s$  ionization continuum above  $\approx 295$  eV might, for instance, be due to a small fraction of carbon  $1s$  vacancies that decay radiatively, i.e. without subsequent emission of an Auger electron: For atomic carbon,  $1s$  Auger processes typically have decay rates in the  $10^{14} s^{-1}$  range, whereas radiative decay rates are in the  $10^{12} s^{-1}$  range [45].

The right column in Fig. 2 displays the corresponding data for NDDI into tricationic species. As already discussed, the most straightforward pathway towards double electron removal into the trication is direct carbon  $1s$  ionization, followed by single Auger electron emission. All three spectra feature a strong step-like increase between 294 eV ( $cor^+$ ) and 295 eV ( $ant^+$ ) that corresponds to the ionization threshold. For higher photon energies, a plateau is reached.

Below the ionization threshold, all three spectra exhibit the same resonance features as observed for NDSI. This is a commonly observed phenomenon [22], that is, for instance, explained by double Auger decay, i.e. the C  $1s$  vacancy decay that involves the emission of two Auger electrons. Roos et al. have recently shown

that the C  $1s$  Auger decay in molecules like acetylene ( $C_2H_2$ ), ethylene ( $C_2H_4$ ) and ethane ( $C_2H_6$ ) has an 8 % to 9% probability of double Auger decay [46].

However, the NDDI data in Fig. 2 show an interesting phenomenon. As expected, the ratio between resonant peaks and direct ionization plateau is relatively small for both  $ant^+$  (d) and  $py^+$  (e), as expected from the low probability for double Auger decay. For  $cor^+$  (f) on the other hand, the  $1s-\pi^*$  resonance has higher yields than the ionization continuum. Dramatically different percentages of double Auger decay for the three PAH cations are not likely. Another effect that could contribute to double ionization below the ionization threshold is ‘ionization from within’, i.e. (single) Auger electron emission where the outgoing Auger electron ionizes another site of the molecule [42]. This effect naturally scales with the size of the molecule.

In order to compare NEXAMS data for all 5 molecular cations under study, Fig. 3 shows spectra based on partial ion yields (PIYs) for the most intense monocationic fragments ( $ant$ :  $C_6H_4^+$ ;  $py$ :  $C_7H_3^+$ ;  $hpy$ :  $C_5H_3^+$ ;  $tpl$ :  $C_3H_3^+$ ;  $cor$ :  $C_7H_1^+$ ). For all fragmentation channels under study, the resonances in the excitation regime are observed which have been discussed in the last section. It is also obvious that all fragments feature substantial yields in the ionization regime, above the ionization threshold, i.e. both dicationic and tricationic intermediates contribute to the formation of these fragment ions.

In order to interpret the NEXAMS data, we have performed TD-DFT calculations to calculate the oscil-

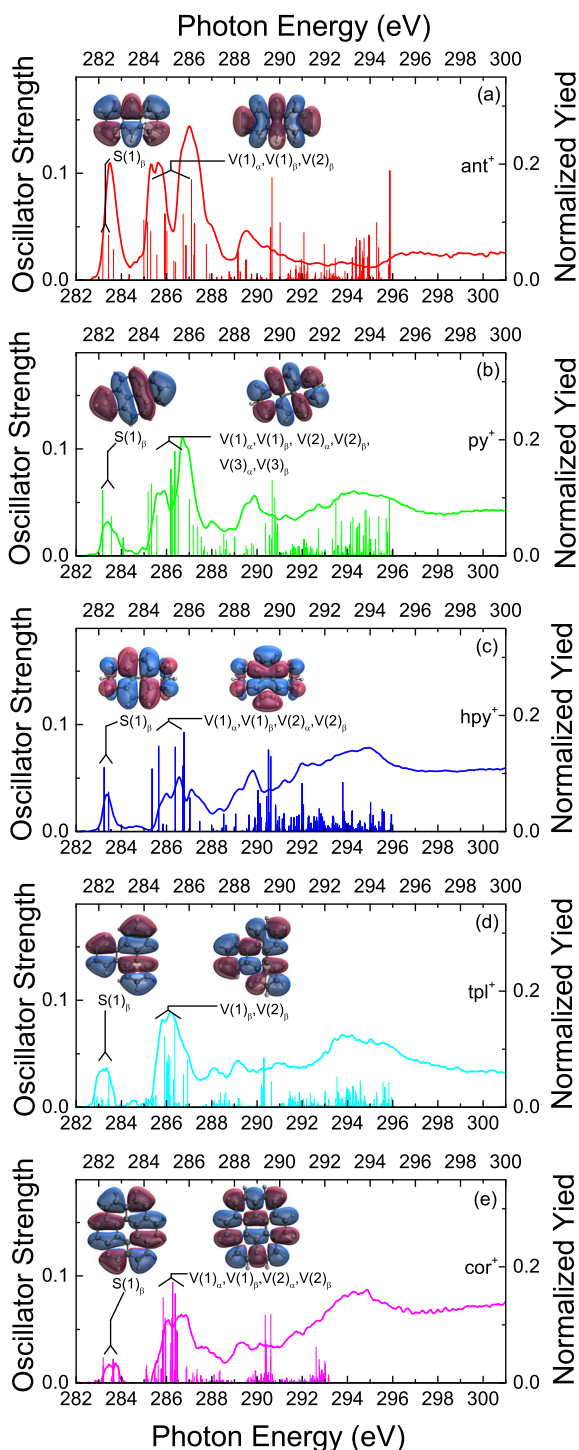


**Fig. 3** NEXAMS data for particularly intense fragment ions **a**  $C_6H_4^+$ ; **b**  $C_7H_3^+$ ; **c**  $C_5H_3^+$ ; **d**  $C_3H_3^+$ ; **e**  $C_7H_1^+$  following photoabsorption by **a**  $ant^+$ , **b**  $py^+$ , **c**  $hpy^+$ , **d**  $tpl^+$  and **e**  $cor^+$ . The calculated oscillator strengths are given as a stick spectrum. Left y-axes: oscillator strengths; right y-axes: normalized experimental NEXAMS intensity; bottom x-axes: energies for theoretical data; and top x-axes: energies for experimental data. Note the 1 eV shift needed to line up experimental axis and theoretical spectra. Selected final states that strongly contribute are presented as isosurface plots. A complete list of isosurface plots can be found in the supplementary material

lator strengths for carbon 1s transitions. The results are shown as stick spectra in Fig. 3. The typical  $\pi^*$  character can be observed in the final state  $S(1)_\beta$  SOMO orbital for all PAH cations. The differences in relative intensity of the SOMO peak (282.5 eV experimentally) might be due to the differences in effective temperature after the photoabsorption process. For  $ant^+$ , 1s-SOMO excitations can already induce substantial fragmentation, for instance, into  $C_6H_4^+$ , whereas this appears to be much less likely for the largest of the 5 PAHs studied  $cor^+$ .

Between 284 eV and 287 eV, transitions to the virtual  $\pi^*$  orbitals  $V(1)_\alpha$ ,  $V(1)_\beta$ ,  $V(2)_\alpha$  and  $V(2)_\beta$  are observed, with double peak structures for  $ant^+$  and  $py^+$  and with a broad transition band for  $hpy^+$ ,  $tpl^+$  and  $cor^+$ . For  $tpl^+$ , only  $V(1)_\beta$  and  $V(2)_\beta$  contribute. At higher photon energies, states with  $\sigma^*$  character start to contribute more strongly.

The relative strength of the ionization continuum is very much dependent on molecular size and structure. For  $ant^+$ , only weak intensity is observed above 292 eV. Very likely, this small cation breaks up into even smaller fragments upon double electron removal. To a smaller extent, this is also true for  $py^+$ . The other 3 molecular ions under study exhibit relatively high intensities above the 1s ionization threshold.

### 3.3 Photofragmentation channels

In the following, we will look more thoroughly into backbone fragmentation of the PAH cations under study. Figure 4 illustrates the differences in carbon backbone fragmentation by 1s excitation (at  $E_{X-ray} = 285$  eV) and 1s ionization (at  $E_{X-ray} = 300$  eV). PIYs for groups of fragment ions with a common number of carbon atoms  $N$  are displayed. For monocationic fragments, these are the sums of peaks  $C_NH_n^+$ . For dicationic and tricationic photoproducts with intact carbon backbones, we display the respective precursor dications and trications with and without H-losses, as well as fragment dications  $C_NH_n^{2+}$ , in case their yields are sufficiently high.

The comparison of the data from  $ant^+$ ,  $py^+$  and  $cor^+$  [ $T_{eff} \sim 2050$  K ( $ant^+$ ), 1940 K ( $py^+$ ) and 1650 K ( $cor^+$ )] shows the expected trends. With decreasing effective temperature, fragmentation is decreasing and the fragmentation pattern is shifting to larger  $N$ .

However, for the three species with almost identical size/ $T_{eff}$  ( $py^+$ ,  $hpy^+$  and  $tpl^+$ ) vast differences in backbone fragmentation are observed, with  $py^+$  having lowest fragment PIYs and sizeable survival of dications and trications with intact backbone. For  $hpl^+$ , no dications and trications with intact backbone are observed. However, relatively large dications that only lost one or few C atoms are still observed. For  $tpl^+$ , solely multi-fragmentation into small  $N$  fragments is observed.

From Fig. 4, it is clear that 1s ionization at 300 eV instead of 1s excitation at 285 eV shifts the fragmentation pattern to smaller masses for  $ant^+$ ,  $py^+$ ,  $hpl^+$  and for  $cor^+$ . Interestingly, for all precursors but  $cor^+$ , frag-

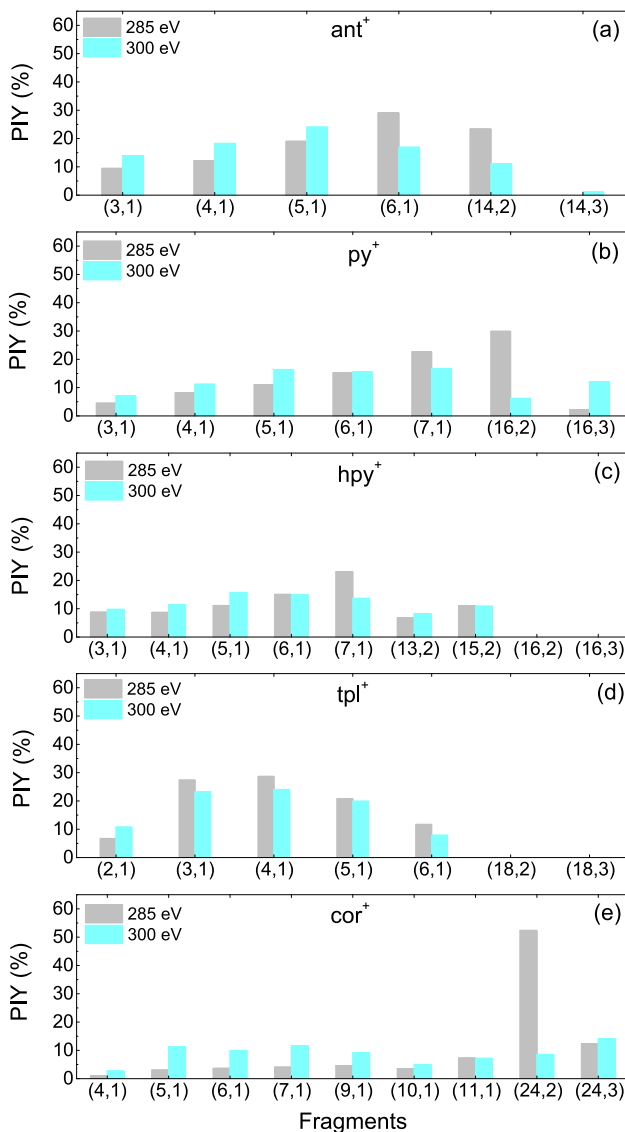


**Fig. 4** PIYs of  $C_NH_n^{z+}$  for soft X-ray photofragments ( $E_{X\text{-ray}} = 285$  eV: light grey,  $E_{X\text{-ray}} = 300$  eV: light cyan). The x-axis labels are (N, z) values of major fragments

mentation into monocations is not much higher in the ionization regime. Only  $cor^+$  shows substantially higher monocation fragment yields at 300 eV for all  $N$  under study.  $tpl^+$  (where solely very relatively small fragments are formed) monocationic fragment yields are lower in the 1s ionization regime, with the exception of  $N = 2$ . Most likely, this PAH cation has such a low structural integrity that 1s ionization leads to a strong increase in very small fragments with masses below the low-mass cut-off of the ion trap.

The conclusion of this section is again that the stability of the carbon backbone not only depends on the effective temperature of the molecular ion, but can be dominated by structural properties. Pericondensed PAHs are clearly more stable than non-pericondensed species. Hydrogen attachment (from  $py^+$  to  $hpy^+$ ) decreases the stability of  $py^+$ , in contrast to what was

earlier observed for  $cor^+$  [24]. The carbon skeleton of  $hpy^+$  is entirely destroyed by X-ray photons. The backbone of  $ant^+$  and  $tpl^+$  is fragile as expected for catacondensed PAH molecules. The structure of  $tpl^+$  is most open and features the most fragile carbon backbone.

### 3.4 Astrophysical implications: the photostability of PAH in XDR

PNe are common carbon-rich environments where PAH evolution is likely. NGC 7027 is a carbon-rich PN, located about 920 parsecs from earth and very bright in the visual range. IR emission from NGC 7027 exhibits the typical features assigned to PAHs [47]. Data from the SOFIA telescope even allowed for mapping spatial distributions of the  $6.2 \mu\text{m}$  PAH emission feature [47], indicating efficient PAH formation from large grains. NGC 7027 is a very high-temperature PN featuring bright soft X-ray emission in the 0.2–3 keV band [8]. It is an open question whether or not PAHs can survive in such environments. In the following, we will therefore investigate, how soft X-ray absorption influences half-life of PAH in this PN.

Here, we only consider non-dissociative photoionization and photodissociation as possible relaxation channels. Other channels such as fluorescence and collision-induced relaxation only contribute marginally. Photodissociation can be further subdivided into carbon backbone fragmentation and H-loss. The absorption cross section  $\sigma_{lu}$  for transitions from a lower state  $|l\rangle$  to an upper excited state  $|u\rangle$  can thus be approximated as the sum of the experimentally observable cross sections for non-dissociative photoionization  $\sigma_{\text{NDI}}$ , for carbon backbone fragmentation  $\sigma_{\text{C-bb}}$  and for H-loss  $\sigma_{\text{H-loss}}$ .

$$\sigma_{lu} = \sigma_{\text{NDI}} + \sigma_{\text{C-bb}} + \sigma_{\text{H-loss}} = \frac{\pi e^2}{m_e c} \cdot f_{lu} \cdot \phi \quad (1)$$

with the oscillator strength  $f_{lu}$  for the transition between  $|l\rangle$  and  $|u\rangle$ , the Maxwellian profile of the transition  $\phi$ , the electron mass  $m_e$ , the elementary charge  $e$  and the speed of light  $c$  [48].

The photoabsorption rate  $k_{\text{abs}}$  for a given molecule is defined as the sum of the product of theoretically determined cross section ( $\sigma_{lu}$ ) and photon flux ( $F_{X\text{-ray}}$ ) [7, 49] for photon energies between  $E_i$  and  $E_f$ :

$$k_{\text{abs}} = \int_{E_i}^{E_f} \sum_{l,u} \sigma_{lu}(E) \cdot F_{X\text{-ray}}(E) dE \quad (2)$$

The photon flux in the PNe can be approximated as:

$$F_x = \frac{L_{X\text{-ray}}}{4\pi r^2 h\nu} \cdot e^{-\tau_{X\text{-ray}}} \quad (3)$$

where  $L_{X\text{-ray}} = 7 \times 10^{31} \text{erg s}^{-1}$  [10] is the integrated X-ray luminosity and  $r$  represents the distance between the X-ray source and the location within the PNe. The X-ray optical depth is  $\tau_{X\text{-ray}} = \alpha \cdot 4.6 \times 10^{-21} N_{\text{H}_2}$ .

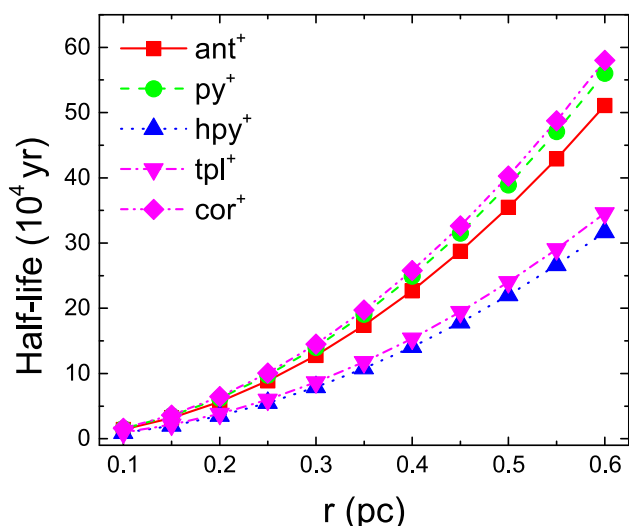


**Fig. 5** The half-lives of 5 PAHs exposed to the NGC 7027 soft X-ray source as the function of distance to the central star ( $r = 0.1 - 0.6$  pc). The  $L_{X-ray} = 7 \times 10^{31}$  erg s<sup>-1</sup>

$(\frac{E}{0.6\text{keV}})^{-2.67}$  [50]. Here, only the interval of C 1s excitations to  $\pi^*$  orbitals in the energy range between 282 eV and 292 eV have been considered because the TD-DFT calculations can only be performed for transitions to bound states. From the comparison of theory and experiment, it is, however, clear that the contribution of the ionization continuum has the same order of magnitude as the resonant part of the spectrum.

In the following, the values of  $\sigma_{lu}$  were computed by TD-DFT. These are to some extent related to the size of the PAH cations under study. The geometrical structure and state of hydrogenation affect  $\sigma_{lu}$  as well.

The second factor affecting half-life of PAH cation is the relaxation channels. Based on the experimentally observed normalized PIYs, e.g. for carbon backbone fragmentation ( $PIY_{C-bb} = \frac{\sigma_{C-bb}}{\sigma_{lu}}$ ), the corresponding absolute cross section can be determined  $\sigma_{C-bb} = \sigma_{lu} \cdot PIY_{C-bb}$ . The half-life of carbon backbone of fragment of interests then becomes  $t_{1/2} = \frac{\ln 2}{k_{C-bb}}$ , and we can define the carbon backbone fragmentation rate:

$$k_{C-bb} = \int_{E_i}^{E_f} \sum_{l,u} \sigma_{lu}(E) \cdot PIY_{C-bb} \cdot F_{X-ray}(E) dE \tag{4}$$

The resulting half-lives for 5 PAHs exposed to the NGC 7027 soft X-ray source are shown in Fig. 5.

All half-lives of studied PAH cations exhibit the trivial increase with distance from the X-ray source  $r$  that reflects the decrease in photon flux. Systematically the highest half-life is observed for  $cor^+$ , followed by  $py^+$  and  $ant^+$ . This order simply reflects the size of these PAHs and their internal temperature. For the species  $hpy^+$  (multiply hydrogenated) and  $tpl^+$  (geometrically very open structure), half-lives are systematically lower by about a factor of 2.

## 4 Conclusions

We have experimentally studied soft X-ray-induced ionization and fragmentation of 5 small PAHs by means of NEXAMS. The experimental data were compared to oscillator strengths obtained by TD-DFT calculations with a SRC functional. Good agreement between experiment and theory was observed. For photon energies around the carbon K-edge, we observed a competition of carbon backbone fragmentation, (multiple) hydrogen loss and non-dissociative ionization. Comparing the frequently investigated PAHs anthracene, pyrene and coronene, we observed a relative decrease of backbone fragmentation and a relative increase of non-dissociative ionization as a function of the number of carbon atoms. This is expected and merely reflects the molecular size dependence of the PAH effective temperature after soft X-ray absorption and subsequent Auger decay. However, when comparing  $py^+$  to  $hpy^+$  and  $tpl^+$ , three PAH cations of very similar size and effective temperature but a very different geometry or hydrogen content, entirely different conclusions can be drawn. The additional H atoms in  $hpy^+$  weaken the carbon backbone, but increase the ability to stabilize positive charge. The very open structure of  $tpl^+$  on the other hand dramatically weakens the PAH structure and facilitates total soft X-ray photofragmentation into very small fragments. This is reflected in pronounced differences in PAH cation survival in astronomical environments. For the conditions in the planetary nebula NGC 7027, we find comparable half-lives for  $ant^+$ ,  $py^+$  and  $cor^+$  and half-lives that are a factor of two shorter for  $hpy^+$  and  $tpl^+$ . The differences in lifetimes cannot easily be explained by a difference in electronic structure, as NEXAFS data for the 5 different systems are very similar. They are rather due to the weaker molecular structure of these molecular cations, which is obvious from the absence of non-dissociative ionization.

**Acknowledgements** We thank HZB for the allocation of synchrotron radiation beamtime. The endstation at UE52-PGM is supported by BMBF grant 05K16VF1. The research leading to this result has been supported by the project CALIPSOplus under the Grant Agreement 730872 from the EU Framework Programme for Research and Innovation HORIZON 2020. Yining Huo acknowledges the funding support by Chinese Scholarship Council (CSC). Shirin Faraji thanks the Innovational Research Incentives Scheme Vidi 2017 with project number 016.Vidi.189.044, which is financed by the Dutch Research Council (NWO). The authors thank the Center for Information Technology of the University of Groningen, which provides the Peregrine high-performance computing cluster. The authors would like to acknowledge the contribution of the EU COST action MD-GAS (CA18212). The COFUND project oLife has received funding from the European Union's Horizon 2020 research and innovation programme under grant agreement No 847675. The authors acknowledge Dr. Francis Penent for sharing Auger spectroscopic data.

## Author contributions

YH and TS contributed to conceptualization; YH, TS, MKEC, SF and VZ-B were involved in methodology; YH, MKEC, VZ-B, MK, MT, SF and TS contributed to formal analysis and investigation; YH, MKEC and TS were involved in writing—original draft preparation; YH, MKEC, VZ-B, SF, BL, RH and TS contributed to writing—review and editing; TS, SF, JTL and BI were involved in funding acquisition; TS, JTL, BI and SF contributed to resources; and TS, SF, RH, JTL and VZ-B were involved in supervision.

**Data Availability Statement** This manuscript has associated data in a data repository. [Authors' comment: Data sets generated during the current study are available from the corresponding author on reasonable request.]

**Open Access** This article is licensed under a Creative Commons Attribution 4.0 International License, which permits use, sharing, adaptation, distribution and reproduction in any medium or format, as long as you give appropriate credit to the original author(s) and the source, provide a link to the Creative Commons licence, and indicate if changes were made. The images or other third party material in this article are included in the article's Creative Commons licence, unless indicated otherwise in a credit line to the material. If material is not included in the article's Creative Commons licence and your intended use is not permitted by statutory regulation or exceeds the permitted use, you will need to obtain permission directly from the copyright holder. To view a copy of this licence, visit <http://creativecommons.org/licenses/by/4.0/>.

## References

1. A.G.G.M. Tielens, *Ann. Rev. Astron. Astrophys.* **46**, 289 (2008)
2. H. Zettergren et al., *Eur. Phys. J. D.* **75**, 152 (2021)
3. R. Chacko, S. Barik, S. Banhatti, G. Aravind, *Phys. Rev. A* **105**, 032804 (2022)
4. J. Zhen, S.R. Castillo, C. Joblin, G. Mulas, H. Sabbah, A. Giuliani, L. Nahon, S. Martin, J. Champeaux, P.M. Mayer, *Astrophys. J.* **822**, 113 (2016)
5. J. Zhen, P. Castellanos, D.M. Paardekoopje, N. Ligtnerink, H. Linnartz, L. Nahon Laurent, C. Joblin, A.G.G.M. Tielens, *Astron. Astrophys.* **804**, L7 (2015)
6. A. Marciniak, C. Joblin, G. Mulas, V.R. Mundlapati, A. Bonnamy, *Astron. Astrophys.* **652**, A42 (2021)
7. H.M. Quiján-Lara, F. Fantuzzi, M.A.C. Nascimento, W. Wolff, H.M. Boechat-Roberty, *Astrophys. J.* **854**, 61 (2018)
8. J.H. Kastner, S.D. Vrtilik, N. Soker, *Astrophys. J.* **550**, L189 (2001)
9. Y. Zhang, K. Sun, D.V. Trung, *Astrophys. J.* **678**, 328 (2008)
10. R. Mentez, J.H. Kastner, *Astrophys. J.* **861**, 45 (2018)
11. J. Vink, *Astron. Astrophys. Rev.* **20**, 49 (2012)
12. L.M. Oskinova, V.V. Gvaramadze, G. Gräfener, N. Langer, H. Todt, *Astron. Astrophys.* **644**, L8 (2020)
13. E. Jiménez-Bailón, M. Santos-Lleó, M. Dahlem, M. Ehle, J.M. Mas-Hesse, M. Guainazzi, T.M. Heckman, K.A. Weaver, *Astron. Astrophys.* **442**, 861 (2005)
14. S. Aalto, S. Müller, K. Sakamoto, J.S. Gallagher, S. Martín, F. Costagliola, *J. Chem. Phys.* **546**, A68 (2012)
15. F. Costagliola, R. Herrero-Illana, A. Lohfink, M. Pérez-Torres, S. Aalto, S. Müller, A. Alberdi, *Astron. Astrophys.* **594**, A114 (2016)
16. S. Puccetti, A. Comastri, F.E. Bauer, W.N. Brandt, F. Fiore, F.A. Harrison, B. Luo, D. Stern, C.M. Urry, D.M. Alexander, A. Annuar, P. Arévalo, M. Baloković, S.E. Boggs, M. Brightman, E.E. Christensen, W.W. Craig, P. Gandhi, C.J. Hailey, M.J. Koss, S. La Massa, A. Marinucci, C. Ricci, D.J. Walton, L. Zappacosta, W. Zhang, *Astron. Astrophys.* **585**, A157 (2016)
17. D. Salak, Y. Tomiyasu, N. Nakai, N. Kuno, Y. Miyamoto, H. Kaneko, *Astrophys. J.* **856**, 97 (2018)
18. C. Rab, M. Güdel, P. Woitke, I. Kamp, W.F. Thi, M. Min, G. Aresu, R. Meijerink, *Astrophys. J.* **609**, A91 (2018)
19. L. Gavilan, P.J. Ho, U. Gorti, H. Ogasawara, C. Jäger, F. Salama, *Astrophys. J.* **925**, 86 (2022)
20. G. Reitsma, L. Boschman, M.J. Deuzeman, O. González-Magaña, S. Hoekstra, S. Cazaux, R. Hoekstra, T. Schlathölter, *Phys. Rev. Lett.* **113**, 053002 (2014)
21. G. Reitsma, L. Boschman, M.J. Deuzeman, S. Hoekstra, R. Hoekstra, T. Schlathölter, *Astron. Astrophys.* **142**, 024308 (2015)
22. Y. Huo, M. Espinoza Cangahuala, M. Goullart, V. Zamudio-Bayer, M. Kubin, M. Timm, B. von Issendorff, J.T. Lau, R. Hoekstra, S. Faraji, T. Schlathölter, *Phys. Rev. A* **106**, 063104 (2022)
23. O. González-Magaña, G. Reitsma, M. Tiemens, L. Boschman, R. Hoekstra, T. Schlathölter, *J. Phys. Chem. A* **116**, 10745 (2012)
24. Y. Huo, M. Espinoza Cangahuala, V. Zamudio-Bayer, M. Goullart, M. Timm, B. von Issendorff, J.T. Lau, R. Hoekstra, S. Faraji, T. Schlathölter, *Mon. Not. R. Astron. Soc.* **523**, 865 (2023)
25. M.H. Stockett, L. Avaldi, P. Bolognesi, J.N. Bull, L. Carlini, E. Carrascosa, J. Chiarinelli, R. Richter, H. Zettergren, *Astrophys. J.* **913**, 46 (2021)
26. M. Wolf, H.V. Kiefer, J. Langeland, L.H. Andersen, H. Zettergren, H.T. Schmidt, H. Cederquist, M.H. Stockett, *Astrophys. J.* **832**, 24 (2016)
27. R. Lindblad, L. Kjellsson, R.C. Couto, M. Timm, C. Bülow, V. Zamudio-Bayer, M. Lundberg, B. von Issendorff, J.T. Lau, S.L. Sorensen, V. Carravetta, H. Ågren, J.E. Rubensson, *Phys. Rev. Lett.* **124**, 203001 (2020)
28. K. Hirsch, J.T. Lau, P. Klar, A. Langenberg, J. Probst, J. Rittmann, M. Vogel, V. Zamudio-Bayer, T. Möller, B. von Issendorff, *J. Phys. B: At. Mol. Opt. Phys.* **42**, 154029 (2009)
29. N.A. Besley, J.C.P. Michael, D.J. Tozer, *Phys. Chem. Chem. Phys.* **11**, 10350 (2009)
30. N.A. Besley, F.A. Asmuruf, *Phys. Chem. Chem. Phys.* **12**, 12024 (2010)
31. E. Epifanovsky et al., *J. Chem. Phys.* **155**, 084801 (2021)
32. S. Hirata, M. Head-Gordon, *Chem. Phys. Lett.* **314**, 291 (1999)

33. R. Wehlitz, J. Phys. B: At. Mol. Opt. Phys. **49**, 222004 (2016)
34. D. Egorov, L. Schwob, M. Lalonde, R. Hoekstra, T. Schlathölter, Phys. Chem. Chem. Phys. **18**, 26213 (2016)
35. R. Spohr, T. Bergmark, N. Magnusson, L.O. Werme, C. Nordling, K. Siegbahn, Phys. Scr. **2**, 31 (1970)
36. S. Carniato, P. Selles, A. Ferté, N. Berrah, A.H. Wuosmaa, M. Nakano, Y. Hikosaka, K. Ito, M. Žitnik, K. Bučar, K. Soejima, K. Jänkälä, D. Cubaynes, J.-M. Bizau, L. Andric, M.A. Khalal, J. Palaudoux, P. Lablanquie, F. Penent, J. Phys. B: At. Mol. Opt. Phys. **53**, 244010 (2020)
37. E.R. Micelotta, A.P. Jones, A.G.G. Tielens, Astron. Astrophys. **510**, A37 (2010)
38. A. Legér, P. Boissel, F.X. Désert, L. d'Hendecourt, Astron. Astrophys. **213**, 351 (1989)
39. S. Martin, L. Chen, A. Al-Mogeeth, J. Bernard, Phys. Rev. A **99**, 012712 (2019)
40. J. Postma, R. Hoekstra, A.G.G.M. Tielens, T. Schlathölter, Astrophys. J. **783**, 61 (2014)
41. A.I.S. Holm, H.A.B. Johansson, H. Cederquist, H. Zettergren, J. Chem. Phys. **134**, 044301 (2011)
42. S. Bari, D. Egorov, T.L.C. Jansen, R. Boll, R. Hoekstra, V. Zamudio-Bayer, C. Bülow, R. Lindblad, G. Leistner, A. Ławicki, K. Hirsch, P.S. Miedema, B.V. Issendorff, J.T. Lau, T. Schlathölter, Chem. Eur. **24**, 7631 (2018)
43. F. Alvarado, S. Bari, R. Hoekstra, T. Schlathölter, Phys. Chem. Chem. Phys. **8**, 1922 (2006)
44. M. Gatchell, M.H. Stockett, N. de Ruelle, T. Chen, L. Giacomozzi, R.F. Nascimento, M. Wolf, E.K. Anderson, R. Delaunay, V. Vizcaino, P. Rousseau, L. Adoui, B.A. Huber, H.T. Schmidt, H. Zettergren, H. Cederquist, Phys. Rev. A **92**, 050702 (2015)
45. M.H. Chen, K.J. Reed, D.M. McWilliams, At. Data Nucl. Data Tables **65**, 289 (1997)
46. A. Hult Roos, J.H.D. Eland, J. Andersson, R.J. Squibb, D. Kolentianos, O. Talaee, R. Feifel, Sci. Rep. **8**, 16405 (2018)
47. R.M. Lau, M. Werner, R. Sahai, M.E. Ressler, Astrophys. J. **833**, 115 (2016)
48. B.T. Draine, *Physics of the Interstellar and Intergalactic Medium* (Princeton University Press, Princeton, 2011)
49. H.M. Quitián-Lara, F. Fantuzzi, R.R. Oliveira, M.A.C. Nascimento, W. Wolff, H.M. Boechat-Roberty, Mon. Not. R. Astron. Soc. **499**, 6066 (2020)
50. S. Deguchi, H. Izumiura, N. Kaifu, Q.R. Nguyen, N. Ukita, Astrophys. J. **351**, 522 (1990)